

Vibration-induced friction modulation for an oscillator moving on an elastic rod

Sulollari, E.; van Dalen, K. N.; Cabboi, A.

DO

10.1016/j.ijsolstr.2025.113572

Publication date

Document VersionFinal published version

Published in

International Journal of Solids and Structures

Citation (APA)

Sulollari, E., van Dalen, K. N., & Cabboi, A. (2025). Vibration-induced friction modulation for an oscillator moving on an elastic rod. *International Journal of Solids and Structures*, *321*, Article 113572. https://doi.org/10.1016/j.ijsolstr.2025.113572

Important note

To cite this publication, please use the final published version (if applicable). Please check the document version above.

Copyright

Other than for strictly personal use, it is not permitted to download, forward or distribute the text or part of it, without the consent of the author(s) and/or copyright holder(s), unless the work is under an open content license such as Creative Commons.

Takedown policy

Please contact us and provide details if you believe this document breaches copyrights. We will remove access to the work immediately and investigate your claim.

ELSEVIER

Contents lists available at ScienceDirect

International Journal of Solids and Structures

journal homepage: www.elsevier.com/locate/ijsolstr



Vibration-induced friction modulation for an oscillator moving on an elastic rod

E. Sulollari *, K.N. van Dalen, A. Cabboi

Department of Engineering Structures, Faculty of Civil Engineering and GeoSciences, Delft University of Technology, Stevinweg 1, 2628CN Delft, Netherlands

ARTICLE INFO

Keywords: Flexible rod Effective friction Model expansion Geometrical nonlinearity Critical velocity Slip joint

ABSTRACT

Several studies have been dedicated to altering friction forces, with external excitation being one of the approaches explored. When the latter is considered, its influence has primarily been studied within the context of discrete systems. Therefore, in this study, a moving oscillator in frictional contact with an elastic rod of finite length subjected to distributed damping is considered, to study the influence of external excitation in the presence of support flexibility on friction modulation. The modal expansion method is used to derive the modal equations of motion, which are then solved numerically. Two cases are investigated, one with the load acting on the mass and the other with the load acting on the rod. It is found that, for both cases, friction modulation varies along the rod's length, and it differs from that obtained assuming a rigid rod. Moreover, for the load-on-mass scenario, a critical velocity is defined, providing direct insight into the friction modulation differences between flexible and rigid rod cases. For the load-on-rod scenario, large deformations are observed close to and above resonance, and geometric nonlinearity is accounted for to describe the system dynamics accurately. To link theoretical results to applications, the findings are used to qualitatively interpret slip-joint vibration-assisted decommissioning tests, and are compared with experimental results in which friction force reduction is explained through the use of elasto-plastic friction models that account for surface deformability, showing good qualitative agreements between the theoretical and experimental outcomes.

1. Introduction

Controlling the tribological behaviour of interfaces is essential for the satisfactory operation of systems in many fields of applied science. This control is crucial for mitigating energy, efficiency and economic losses and reducing noise pollution (Liu et al., 2022). Tribological interface properties encompass various factors, including surface roughness, hardness, wear, and friction. Over the past few decades, extensive research has explored ways to modulate or control friction forces without relying on lubricants. This area of study is particularly relevant in mechanical engineering, as lubrication management — such as timely application, removal, and replacement - can be both challenging and labour-intensive. Additionally, the environmental impact of lubricants further underscores the importance of developing alternative frictioncontrol strategies. A lubricant-like effect at the sliding interface can also be reproduced by a surrounding oscillatory field. The use of a deliberate application of oscillatory forces has already been implemented in metal working (Siegert and Möck, 1996), decommissioning of joints (Cabboi et al., 2021), positioning control in robots (Ipri and Asada, 1995), pile driving (Tsetas et al., 2023) and rendering textures in surface haptics (Meyer et al., 2014). However, besides the scope of controlling

a sliding process, the presence of an oscillatory field at the sliding interface (if uncontrolled or if mistakenly neglected), can also lead to erroneous interpretations of measured friction forces, if the goal is to assess the tribological behaviour of a sliding interface. This may result in an apparent (but misleading) dependency between the friction force and the sliding velocity (Tolstoi, 1967; Soom and Kim, 1983). The complexity of the friction-vibration interaction increases if the influence of the so-called "inner-dynamics" of the interface is introduced. In fact, in previous studies (Hess et al., 1992; Grudziński and Kostek, 2007; Costagliola et al., 2017, 2018; Menga et al., 2021, 2023), it has been shown that the small-scale dynamics of a micro-structured interface can have a substantial effect on friction modulation. This means that a desired frictional behaviour can also be obtained by optimizing the properties of the microstructure. Besides the application of modulating the friction force, the use of a deliberate high-frequency microvibration was also investigated to control the adhesion behaviour between two material pairs (Tricarico et al., 2025; Argatov et al., 2025), a topic that lies beyond the remit of this study.

E-mail addresses: E.Sulollari@tudelft.nl (E. Sulollari), K.N.vanDalen@tudelft.nl (K.N. van Dalen), A.Cabboi@tudelft.nl (A. Cabboi).

^{*} Corresponding author.

Over the last two decades, researchers have used various models to study friction modulation, with a special focus on developing strategies to quench friction-induced instabilities of a sliding system, the simplest one being represented by a single-degree-of-freedom oscillator sliding over a rigid belt. The effect of a high-frequency tangential excitation on such model was studied by Thomsen (Thomsen, 1999), who showed that high-frequency excitation can prevent self-excited oscillations by effectively cancelling the negative slope in the assumed friction-velocity relationship. Follow-up studies were carried out by Michaux and coworkers (Michaux et al., 2007) in which monotonic and non-monotonic friction-velocity relations were assumed. An extension to the two-degree-of-freedom system was investigated by Hoffman and coworkers (Hoffmann et al., 2005). In their work, they not only investigated the effect of external tangential excitation on the friction force change, but also showed that excitation can stabilize the modecoupling instability. Other studies used similar systems, emphasizing the focus on the stability rather than friction modulation (Ouyang et al., 1999; Sinou and Jezequel, 2007; Li et al., 2016; Hong et al., 2020). In a more recent study, Sulollari and coworkers also considered a similar system to study both the friction modulation and the system stability under the effect of parametric excitation (Sulollari et al., 2025).

The above-mentioned studies did not account for the effect caused by microstructured surfaces, whose corresponding stiffness and dynamic properties can significantly affect the friction force. This is shown by Costagliola and coworkers (Costagliola et al., 2017), who considered a 1-D elastic surface discretized into mass elements connected by springs, a discretization representative of the microscopic heterogeneity of the surface roughness. A 2-D spring-block model was studied in a follow-up study (Costagliola et al., 2018). Both models showed that the frictional behaviour depends strongly on the microstructures' shape, size and orientation. Menga and coworkers also considered a micro-structured 2-D surface modelled through masses connected to radial and torsional elastic elements (Menga et al., 2021). It was found that different dynamic regimes that affect friction behaviour can be achieved depending on the supports' elastic properties and static orientation. In a follow-up study, the frictional behaviour of a 3-D lattice structure was studied to account for the effect of the local distribution of the normal load and the in- and out-of-plane self-excited vibrations emergence (Menga et al., 2023). These studies show that by optimizing the mechanical properties of the interface microstructure, it would be possible to obtain the desired friction behaviour.

Other than theoretical studies examining the effect of external excitation or microstructure dynamics on friction modulation and stability, numerous experimental studies with similar objectives have also been conducted, the results of which have been compared using models (discrete and continuous) akin to those described earlier. Commonly, the experimental tests are conducted on pin-on-disk setups. For instance, Littmann and coworkers (Littmann et al., 2001), Storck and coworkers (Storck et al., 2002) and Kumar and Hutchings (Kumar and Hutchings, 2004) studied the reduction of the friction force due to ultrasonic vibrations applied parallel and perpendicularly to the sliding direction. For each loading case, qualitative agreements between theoretical predictions (e.g., based on single-degree-of-freedom systems) and measurements (e.g., involving a moving ultrasonic vibrator along a track) were obtained. A better consistency of the experimental and theoretical results was obtained by Tsai and Tseng (Tsai and Tseng, 2006) using the Dahl model (Dahl, 1976) which takes into account contact deformability in the tangential direction, or the elasto-plastic friction model proposed by Dupont and coworkers (Dupont et al., 2002). Kapelke also used the Dupont model and the Amontons-Coulomb law to compare the experimental results to theoretical ones and found an excellent match between the experimental and theoretical results for tests carried out with moderate excitation frequencies (Kapelke and Seemann, 2018). Thus, when comparing experimental results to theoretical studies, the latter are typically focused on 1- or 2-DOF

systems, utilizing friction models often coupled with terms accounting for the surface compliance (see the use of the Dahl or Dupont model). Besides small-scale experiments, the notion of modulating a friction force through a deliberate oscillatory forcing has also been applied to large-scale structures. More specifically, a vibration-assisted technique was tested through laboratory experiments to modulate the friction force, enabling the installation and removal of a scaled slip joint (Cabboi et al., 2020). A follow-up study applied the technique on a full-scale slip joint for a wind turbine connection (Cabboi et al., 2021), allowing the decommissioning of the slip joint itself. While the decommissioning operations successfully confirmed the effectiveness of the vibration-assisted technique and correlations were established between the excitation frequencies used and the structural modes of vibration, the actual change of the friction force due to the applied excitation could not be quantified. Moreover, analysing a more realistic (or high-fidelity) model of the large-scale structure with friction-vibration interaction proved to be too complex for understanding the observed physical behaviour.

While previous studies have investigated the effect of external excitation on friction modulation using discrete systems or focused on the influence of microstructure dynamics and geometry without considering external excitation, there remains a gap in understanding how external excitation interacts with the dynamics of continuous systems, which are more representative of the dynamics of real systems. Therefore, this study aims to analyse the effect of external excitation on friction, considering a moving oscillator on an elastic rod of finite length subjected to distributed damping, which allows for a more realistic representation of how external excitation influences the frictional behaviour through continuous deformations. Two cases are investigated, one with the external load acting on the mass and the other one with the load acting on the rod. For both cases and various excitation frequencies, the values of the effective (or average) friction vary along the rod's length and differ from those obtained assuming a rigid rod. For the load-on-mass scenario, a critical velocity is defined, which reveals direct insight into the differences in friction modulation between the flexible and rigid rod cases. The application of an external excitation to the rod needs particular attention in order to avoid large axial deformation under resonance conditions or highexcitation frequencies. For cases when large deformations are allowed (depending on the material type, properties, loading conditions etc.), geometric nonlinearity is accounted for in the equations of motion. Finally, the results of this study are used to qualitatively explain the vibration-assisted decommissioning tests of the slip joint (Cabboi et al., 2021, 2020), and allow for a comparative discussion with the friction modulation results obtained using elasto-plastic friction models meant to encapsulate the surface deformability (Kapelke and Seemann, 2018).

The paper is structured as follows. First, the description of the moving oscillator on the rod is introduced in Section 2. In Section 3, the results on friction modulation are obtained when the oscillatory load acts on the mass. The results for the load acting on the rod are presented in Section 4. In Section 5, analogies with real-world applications and experimental studies are explored to contextualize the modelling choices. Finally, conclusions are drawn in Section 6 and the Appendix is added, providing additional details to the discussions and the results presented in this study.

2. The model system

To reveal the effects of axial rod deformations on vibration-induced friction modulation, the system illustrated in Fig. 1 is considered. Fig. 1(a) illustrates the case where the harmonic load is applied on the mass, and Fig. 1(b), the case where the load is applied on the rod. The system consists of a moving oscillator composed of a mass m, a spring with stiffness k and a dashpot with damping coefficient c, connected to a massless support. The support is pushed to the right direction with a constant velocity v and the distance from the left end at time t is vt.

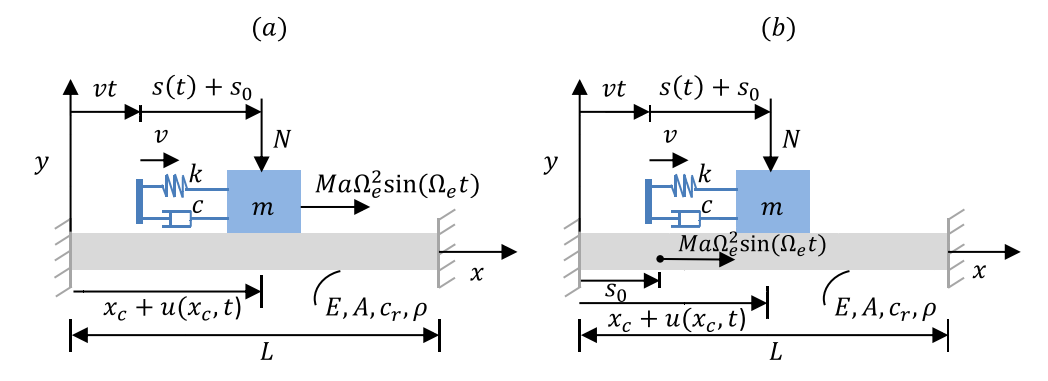


Fig. 1. Oscillator moving on an axially deforming rod: (a) harmonic load applied on the mass; (b) harmonic load applied on the rod at a position defined by the initial length of the spring s_0 .

The initial length of the spring is s_0 and the elongation of the spring from the free length is s. The load N is a constant normal preload acting on the mass. The rod has a cross-sectional area A, density ρ , length L, Young's modulus E and damping coefficient c_b . The axial deformation of the rod at a given position x is u(x,t). The rod has fixed supports on both ends. The external harmonic loading is characterized by a frequency Ω_e and an amplitude $Ma\Omega_e^2$ (e.g., load arising from a horizontally unbalanced mass M at eccentricity a (Thomsen, 1999)). For the load acting on the rod, Fig. 1(b), the application point corresponds to the position defined by the spring's initial length s_0 .

For the chosen model setup, the kinetic friction is considered to be the same as the static friction. The adopted friction law is the Amontons–Coulomb's law (Amontons, 1699; Coulomb, 1821), since the corresponding friction force is directly linked to a constant coefficient of friction, and proportional to the normal force. As the aim of this study is to capture the effect of the rod deformation on vibration-induced friction changes, the assumption of Amontons–Coulomb's law is deemed most appropriate, since it avoids the complexity of more realistic friction laws which are case-study and material pair dependent (Cabboi and Woodhouse, 2018, 2020). The friction force f acting between the mass and the rod is then

$$f = -\mu_v \operatorname{sgn}(\nu_r) N, \tag{1}$$

where μ_s is the static friction coefficient and v_r is the relative velocity. The latter is expressed as

$$v_r = \dot{s} + v - \dot{u}|_{x = x_r},\tag{2}$$

where the overdot represents the total derivative with respect to time and x_a is the position of the point at which the mass contacts the rod.

Under the small deformation theory, so assuming the deformation of the rod and mass to be negligible compared to L and s_0 , respectively, the expression of x_c can be written as

$$x_c(t) = vt + s_0. (3)$$

It should be noted that in the study of Hong and coworkers (Hong et al., 2020) where a similar system is considered, the full kinematic expression for the contact point is used, and reads as follows

$$x_c(t) = vt + s_0 + s(t) - u(x_c(t), t).$$
 (4)

According to this expression, u and x_c are coupled, so the x_c expression is implicit. Under small deformations, however, the contributions from the spring elongation and the rod deformation are negligible, and Eq. (4) can be approximated by Eq. (3). In this study, when small deformations are considered, Eq. (3) is used, significantly reducing the computational time.

The equations of motion of the system without considering the external forcing terms then become

$$\rho A \frac{\partial^2 u}{\partial t^2} + c_b \frac{\partial u}{\partial t} - E A \frac{\partial^2 u}{\partial x^2} + f \delta(x - x_c) = 0,$$
 (5)

$$m\frac{d^2s}{dt^2} + c\frac{ds}{dt} + ks = f. ag{6}$$

with the boundary conditions for a fixed-fixed rod being

$$u = 0$$
 at $x = 0$ and $u = 0$ at $x = L$, (7)

and the friction force as in Eq. (1). In the case of load-on-mass, an additional loading term appears on the right-hand side of Eq. (6) as $M\alpha\Omega_e^2\sin(\Omega_e t)$. For the load-on-rod case, the loading term appears on the right-hand side of the Eq. (5) as $M\alpha\Omega_e^2\sin(\Omega_e t)\delta(x-s_0)$. To generalize the results, the following dimensionless parameters are introduced:

$$t^* = \omega_n t, \quad \omega_n^2 = \frac{k}{m}, \quad \beta = \frac{c}{2m\omega_n}, \quad x^* = \frac{x}{L}, \quad s^* = \frac{s}{L},$$

$$s_0^* = \frac{s_0}{L}, \quad u^* = \frac{u}{L},$$

$$v^* = \frac{v}{L\omega_n}, \quad v_r^* = \frac{v_r}{L\omega_n}, \quad \delta^* = L\delta, \quad f^* = \frac{f}{\rho A L^2 \omega_n^2},$$

$$N^* = \frac{N}{\rho A L^2 \omega_n^2},$$

$$\beta_b = \frac{c_b}{2\rho A \omega_b}, \quad \omega_b = \frac{\pi}{L} \sqrt{\frac{E}{\rho}}, \quad r_\omega = \frac{\omega_b}{\omega_n}, \quad r_m = \frac{\rho A L}{m},$$

$$\Omega_e^* = \frac{\Omega_e}{\omega_n}, \quad \alpha^* = \frac{Ma}{mL},$$

$$(8)$$

where r_m is the mass ratio of the rod and the oscillator mass, r_ω is the frequency ratio between the rod's first natural frequency and the oscillator's natural frequency (defined for the separate subsystems when no interaction is present) and the asterisk denotes a dimensionless component. Substituting Eq. (8) into Eq. (5) and (6), and dropping the asterisks from the dimensionless equation for simplicity, the dimensionless equations of motion of the unforced system are derived

$$\frac{\partial^2 u}{\partial t^2} + 2\beta_b r_w \frac{\partial u}{\partial t} - \left(\frac{r_w}{\pi}\right)^2 \frac{\partial^2 u}{\partial x^2} + f \delta(x - x_c) = 0, \tag{9}$$

$$\frac{d^2s}{dt^2} + 2\beta \frac{ds}{dt} + s = r_m f. \tag{10}$$

To solve the equations of motion, first, the modal expansion method is used to derive the modal equation from the rod equation. Using this method and the mode shapes of a fixed-fixed rod, the response u(x,t) is written as

$$u(x,t) = \sum_{j=1}^{p} T_j(t) \sin(j\pi x),$$
(11)

where p is the total number of modes considered and $T_j(t)$ is the unknown function of time to be determined. Substituting Eq. (11) into Eqs. (9) and (10), with f and x_c as in Eqs. (1) and (3), respectively, and using the orthogonality property of the mode shapes, the modal equations are obtained

$$\ddot{T}_i + 2\beta_b r_w \dot{T}_i + j^2 r_\omega^2 T_i + 2f_i(\dot{s}, \dot{T}_1, \dot{T}_2 ... \dot{T}_p) = 0, \tag{12}$$

$$\ddot{s} + 2\beta \dot{s} + s - r_m f_i(\dot{s}, \dot{T}_1, \dot{T}_2...\dot{T}_n) = 0.$$
(13)

The modal forces f_i are functions of \dot{s} , \dot{T}_1 , \dot{T}_2 , ..., \dot{T}_n and are given by

$$f_j(\dot{s}, \dot{T}_1, \dot{T}_2...\dot{T}_p) = -\mu_s \operatorname{sgn}(v_r|_{x=x_c}) N \sin(j\pi x_c),$$
 (14)

and

$$v_r|_{x=x_c} = \dot{s} + v - \sum_{i=1}^p \dot{T}_j \sin(j\pi x_c) - \sum_{i=1}^p T_j j\pi \dot{x}_c \cos(j\pi x_c). \tag{15}$$

In the v_r expression, the chain rule is used to calculate the total derivative of \dot{u} since x_c is time dependent. However, the contribution of the last term appeared negligible for the cases considered in this study.

3. Harmonic load acting on the mass

This section examines the case of the external harmonic load acting on the mass, as shown in Fig. 1(a). The equations of motion are solved numerically, and the friction modulation is evaluated as the mass moves along the rod, considering different excitation frequencies. Then, plots of friction modulation for different pushing velocity values v are presented. All results are compared to those obtained for a mass–spring-dashpot system on a rigid rod (analogous to a mass–spring-dashpot on a moving belt system as described in Sulollari et al. (2024)).

3.1. Friction modulation along the rod length

The equations of motion, Eqs. (12) and (13), are solved using the MATLAB solver ode23s, considering $r_{\omega}=6$, $r_{m}=4.8$, $s_{0}=0.25$, $\beta=0.14$, $\beta_{b}=0.001$, $\mu_{s}=0.5$, N=0.002, v=0.005, $\alpha=0.004$ and p=10 (increasing the number of modes can be shown to have a negligible effect on the results). These parameter values are chosen to ensure sliding over a wide range of excitation frequencies. To guarantee that the response adheres to the small deformation assumption, for the parameters chosen, the solutions obtained are compared to those derived considering a rod with geometric nonlinearity, with the x_{c} expression as in Eq. (4). The comparison shows negligible differences between both cases, as demonstrated in Appendix A.1, complying the small deformation assumption.

The mass and rod responses (obtained from Eqs. (12) and (13)) are used to calculate the average friction, $\bar{\mu}(v_r)$, by integrating the friction force over the excitation period as follows

$$\bar{\mu}(v_r) = \left\langle \mu_s \operatorname{sgn}(v_r|_{x=x_c}) \right\rangle = \left\langle \mu_s \operatorname{sgn}(\dot{s} + v - \sum_{j=1}^n \dot{T}_j(t) \sin(j\pi x_c)) \right\rangle, \tag{16}$$

where \ll defines the average operator over the excitation period $\frac{2\pi}{Q}$. In Fig. 2, the continuous lines represent the average friction values obtained for different excitation frequencies as the mass moves along the rod length, ranging from 0.25 to 1, as $s_0 = 0.25$ is chosen. The dot markers represent the average friction values obtained analytically for a mass-spring-dashpot system on a rigid rod/belt as done in Sulollari et al. (2024), where the approach for calculating the average friction through the velocity response function is described. These modulated friction values are constant and do not vary along the length of the rod. The colours of the dot markers correspond to the colours of the continuous lines, indicating that the same parameter values are used for each pair. It should be noted that the initial parts of the continuous lines correspond to oscillation cycles of the transient response as the averaging process is carried out on the entire relative velocity response, whereas the dot markers are obtained analytically considering the steady-state response only.

The results shown in Fig. 2 are obtained for $r_{\omega}=6$, meaning that the natural frequency of the rod's first mode is 6 (i.e. $\omega_b=6$ rad/s and $\omega_n=1$ rad/s). Fig. 2(a) depicts the average friction plots for excitation frequencies smaller than and equal to the rod's first natural frequency, and Fig. 2(b) illustrates results for excitation frequencies exceeding the rod's first natural frequency. Both plots demonstrate that

the continuous lines are not constant, indicating that, unlike the rigid rod case, the rod's flexibility leads to variations in the average friction along its length. Depending on the position along the rod length, these values can be smaller or larger than the ones obtained for the rigid rod. Towards the end of the rod, the values of the continuous lines approach those of the dot markers, since the axial deformation at both rod's ends approaches zero. Differences in values are from rod oscillations in the proximity of the support due to the change in (perceived) stiffness giving rise to transition-radiation effects (Fǎrǎgǎu et al., 2021). While all the continuous lines show variations, the most significant differences relative to the rigid case are observed at excitation frequencies $\Omega_e=3$ and $\Omega_e=6$.

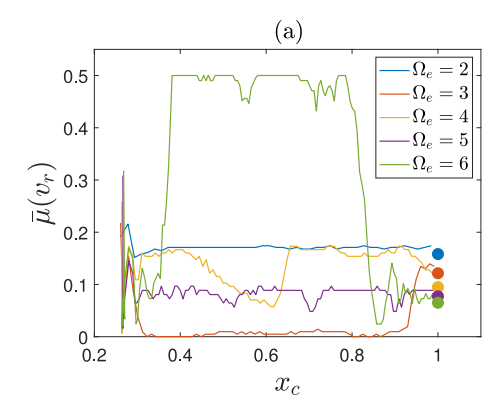
To better highlight the influence of the deformable rod with respect to the rigid one, Fig. 3 shows boxplots for different excitation frequencies, highlighting the statistical distribution of the average friction values while the mass slides over the rod. For each boxplot, the median is indicated by the central red line. The bottom and top edges of the box represent the 25th percentile (Q1) and 75th percentile (Q3), respectively, while the whiskers extend to the most extreme data points within 1.5 times the interquartile range below Q1 and above Q3. All other observed data points outside the boundary of the whiskers are plotted as outliers using the "+" grey marker and are mainly a result of averaging over the oscillation cycles of the transient response.

The green dot markers indicate the average friction values obtained considering the rigid rod and they show a clear trend as their values decrease for increasing excitation frequencies, and for frequencies bigger than the frequency of the rod's first mode, they are close to the median and mean (middle of the box) values of the boxes. For lower excitation values, the green dot markers display significant deviations from the mean and median values represented in the boxes, with the largest discrepancies occurring at excitation frequencies $\Omega_e=3$ and $\Omega_e=6$, as already shown in Fig. 2(a).

Figs. 4 and 5 show the velocity responses of the mass (blue line) and of the rod (red line), for $\Omega_e=3$ and $\Omega_e=6$, respectively. The velocity responses are obtained at the moving contact point and allow us to explain the large deviations observed at these excitation frequencies compared to the rigid rod scenario. The amplitude of the velocity response of the rod in Fig. 5(a) is higher than in Fig. 4(a), as in the former, the excitation frequency corresponds to the frequency of the first mode of the rod. Although the velocity responses have a lower amplitude in Fig. 4(a), the zoom-in in Fig. 4(b) shows the responses to be out of phase with each other. The resulting relative velocity response, v_r , then exhibits a high amplitude, and the friction force reverses direction during each oscillation period. Consequently, this results in low average friction values as shown in Figs. 2(a) and 3.

Fig. 5(b), however, shows the responses to be in phase. The resulting relative velocity has low amplitudes, preventing the friction force from changing direction during certain oscillation cycles. Without a change in direction, the friction force remains constant. This explains why in Fig. 2(a), the average friction tends to the originally imposed friction coefficient $\mu_s=0.5$. Fig. 6(a) illustrates this statement, visualizing the relative velocity obtained for $\Omega_e=6$. Indeed, the amplitudes of the relative velocity response are low and for the time window from ~ 25 –110, the values are mostly positive, meaning the friction force does not change sign. Fig. 6(b), provides a zoom-in where the minimum velocity response value approaches zero, resulting in stick–slip behaviour.

Thus, exciting the mass at an excitation frequency corresponding to the first mode of the rod results in stick–slip behaviour at parts along the rod length, and in a negligible change of the average friction values. Note that for the rigid rod case, stick–slip is not observed. In previous studies (Sulollari et al., 2024, 2025), the average operation was performed when considering continuous sliding as they were focused on analysing friction modulation during sliding only. In this case, however, for $\Omega_e=6$, the averaging process is performed numerically, and it is important to note that this is done over a stick–slip region.



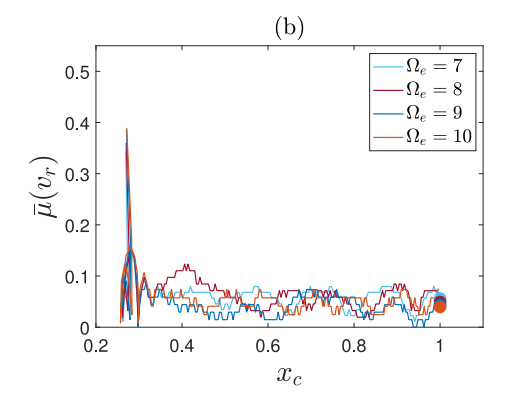


Fig. 2. Average friction results along the rod length for v = 0.005. Continuous lines refer to the case of the flexible rod, and dot markers refer to the rigid rod. Dot marker colours match those of the continuous lines for the same excitation frequency: (a) results for excitation frequencies smaller than and equal to 6, (b) results for excitation frequencies bigger than 6.

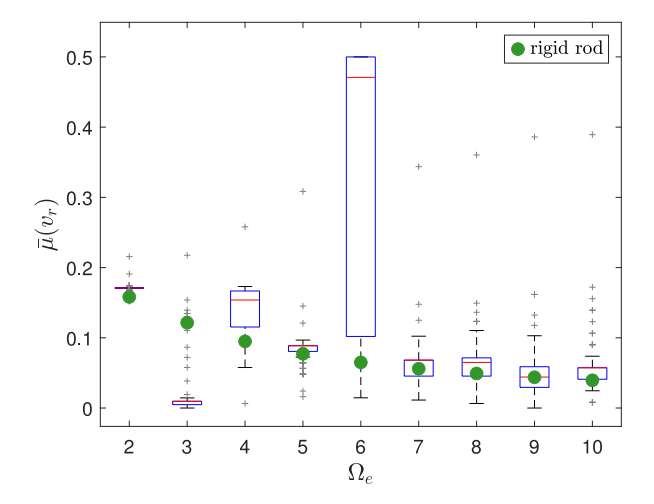


Fig. 3. Comparison between the statistics of the average friction distributions along the rod length (represented by box plots) and the average friction coefficients for the rigid rod. The assumed pushing velocity is v = 0.005.

Before concluding this part, it is worth noting that higher harmonics are present in the rod's velocity response, as shown in Figs. 4 and 5, which arise from the moving nature of the load rather than from the nonlinear contact. It can be verified that in addition to these higher harmonics, which correspond to oscillations at the rod's natural frequencies, the influence of the higher harmonics due to the external excitation is also present (when these do not coincide with the rod's natural frequencies), albeit with a small effect. The presence of all higher harmonics also explains the large variations in the average friction values along x_c , for each excitation frequency, as indicated in Fig. 2. These average friction values are computed by averaging over the oscillation period, $2\pi/\Omega_e$. However, due to the presence of many harmonics, whose relevance varies depending on the x_c positions, the relative velocity response used to calculate the average friction exhibits quasi-periodic behaviour, causing significant variations in the average friction values when averaged over $2\pi/\Omega_e$. While in this study, the averaging is always performed over the period corresponding to the excitation frequency, as discussed in a previous study (Sulollari et al., 2025), when multiple oscillation periods are present in the relative response, the choice of the period is important as it affects the resulting average friction values and their variability.

3.2. Friction modulation versus pushing velocity

This subsection compares the average friction obtained for various pushing velocities v, with reference to the excitation frequencies for

which the most significant difference between the flexible and rigid rod case is observed, i.e. $\Omega_e = 3$ and $\Omega_e = 6$. Fig. 7 depicts the results for $\Omega_e = 3$ for v values ranging from 0.005 to 0.02. As shown in the figure, for low v values (≤ 0.008), the average friction results obtained for the flexible rod are generally smaller than those obtained for the rigid rod, while for bigger v values, the opposite trend holds. For vvalues exceeding the amplitude of the relative velocity response (not presented here), the friction force does not change sign and no friction change is observed ($v \ge 0.014$) for both rigid and flexible rod cases. The figure also suggests the existence of a velocity below which the average friction values for the flexible rod are lower than that of the rigid case, while above it, the opposite is true. To better understand the differences in the average friction values between the flexible and rigid rod cases and to investigate the presence of such transition at a specific velocity, Fig. 8(a) presents the maximum amplitude of the rod velocity at the contact point for each v value. The choice of the rod velocity is based on the fact that the largest difference in relative velocities between the flexible and rigid rods arises from its contribution.

Fig. 8(a) shows that the maximum amplitude of the rod's velocity response is observed at v = 0.008, which corresponds to the velocity for which the trend in the average friction values in Fig. 7 shifts. This value at which the maximum rod velocity occurs is defined as the "critical" velocity and marks the point where the average friction values obtained for the flexible and rigid rod systems are closest to each other. It is worth highlighting that the average friction values being close does not imply that the responses are identical (in fact, they are not, as the rod response is at its maximum while the belt is rigid). It simply means that the change in sign of the relative velocities is similar, resulting in average friction values that are close to each other. For pushing velocities below the critical one, the system with the flexible rod exhibits lower average friction, whereas, for pushing velocities above it, the same system displays higher average friction values (until the velocity for which no friction modulation is observed for both flexible and rigid rod cases). Therefore, identifying the critical velocity offers direct qualitative insight into how the average friction differs between the system with a rigid rod (assuming its average friction is known) and the one with a flexible rod, without the need to explicitly compute the average friction for the latter. Moreover, to explain the increase in average friction values with increasing velocity v and to find the pushing velocity beyond which no friction change is observed, Fig. 8(b) illustrates the minimum relative velocity response value for each v. The $v_{r,\mathrm{min}}$ values decrease, reaching almost zero at v=0.014, meaning that beyond this pushing velocity, the relative velocity values are strictly positive, resulting in a friction force that does not change sign. Consequently, no friction modulation occurs, consistent with the behaviour portrayed in Fig. 7.

Fig. 9 depicts the results for $\Omega_e = 6$ corresponding to the rod's first mode frequency. At low v values, the boxplots show a noticeable

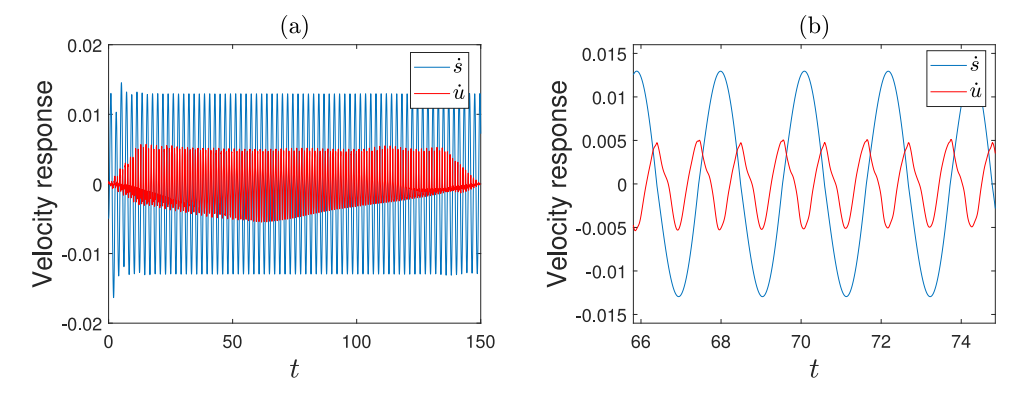


Fig. 4. (a) Mass and rod velocity response in blue and red lines, respectively; (b) Zoom-in on the response. $\Omega_v = 3$ and v = 0.005.

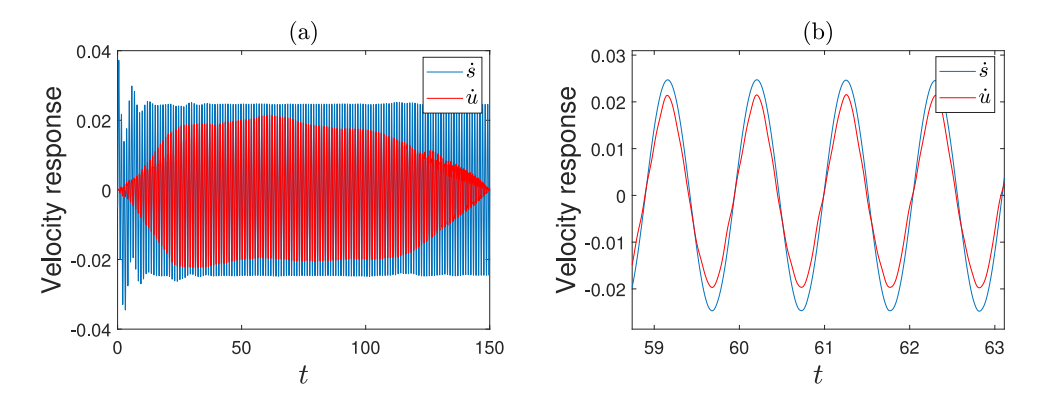


Fig. 5. (a) Mass and rod velocity response in blue and red lines, respectively; (b) Zoom-in on the response. $\Omega_e = 6$ and v = 0.005.

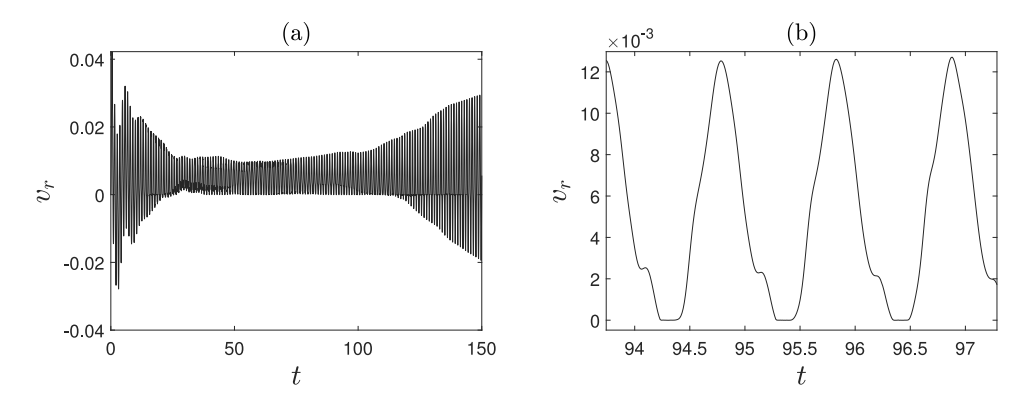


Fig. 6. (a) Relative velocity response for $\Omega_e=6$ and v=0.005; (b) Zoom-in on the relative velocity response indicating stick–slip behaviour.

difference between the mean (middle of the box) and the median as well as a higher spread in the variability of the values. This variability in distribution decreases as v values increase. For all v values, other than the ones for which no friction change is observed, the average friction results for the flexible rod (except for extremes and outliers) are higher than those for the rigid rod case. Thus, independent of the υ value, exciting the mass at an excitation frequency corresponding to the rod's first mode results in less friction reduction. In Fig. 9(b), a plot of $\dot{u}_{\rm max}$ versus v values is presented for this excitation frequency. Unlike Fig. 8(a), no distinct critical velocity is observed within this velocity range, as the $\dot{u}_{\rm max}$ values continuously decrease. This behaviour is similar to the portion of Fig. 8(a) where the velocities are greater than 0.008; there, $\dot{u}_{\rm max}$ also decreases. In Fig. 7, this region is associated with average friction values higher than those of the rigid rod, a pattern consistent with the behaviour shown in Fig. 9(a). Therefore, even for this excitation frequency, the plot of $\dot{u}_{\rm max}$ provides qualitative insights

into the differences in average friction values between the systems with flexible and rigid rods. Notably, it can be verified that the critical velocity defined and calculated in this section is much smaller than the conventional critical velocity corresponding to the resonance of the rod as induced by a moving oscillatory load of frequency Ω_e (see Frýba (1973)).

4. Harmonic load acting on the rod

This section examines the case of the external harmonic load acting on the rod at location $x=s_0$, as shown in Fig. 1(b). Following the methodology and steps outlined in the preceding section, the equations of motion are solved numerically, and the friction modulation is evaluated for different excitation frequencies Ω_e and velocities v. All results are compared to those obtained from a mass–spring-dashpot system on a rigid rod, with the load acting on the mass.

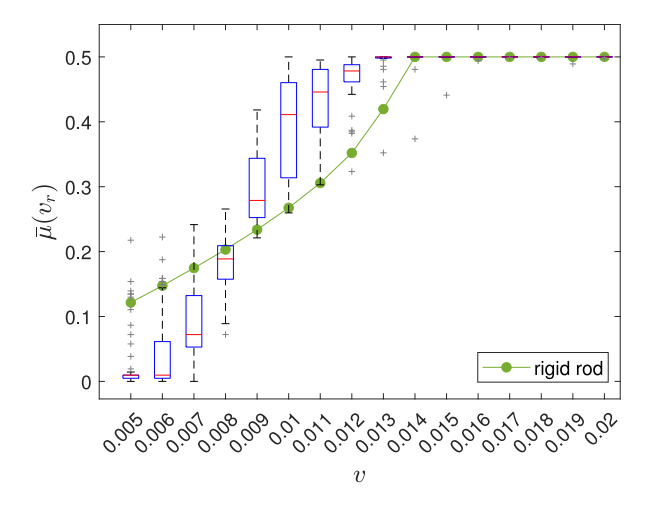


Fig. 7. Comparison of average friction results for different velocity v values obtained for the flexible and rigid rod case for $\Omega_e=3$.

4.1. Friction modulation along the rod length

Using the equations of motion, Eqs. (12) and (13), with the external harmonic loading applied on the rod, first, the average friction values along the rod length are obtained for different excitation frequencies, employing the x_c expression in Eq. (3). The results are depicted in Fig. 10(a) where, like in Fig. 2, the continuous lines represent the results of the flexible rod and the dot markers correspond to those of the rigid rod. Again, similarly to Fig. 2, Fig. 10(a) shows large variations in the average friction values along x_c , for each excitation frequency (other than the ones for which no change in the frictional behaviour is observed, such as for $\Omega_e=2$ and $\Omega_e=3$). For this case as well, with the load acting on the rod, due to the moving load, the beam velocity response exhibits oscillations not only at the excitation frequency but also at additional frequencies, leading to a quasi-periodic response, causing significant variations in the average friction values when averaged over $2\pi/\Omega_e$. The plots in Fig. 10(a) indicate that for $\Omega_e = 2$ and $\Omega_e = 3$ (shown with a dashed line for distinction), no friction change is observed. For $\Omega_e=4$, the average friction values vary along the rod length, and no change is observed after $x_c \approx 0.7$. To explain the constant average friction values after $x_c \approx 0.7$, in Fig. 10(b), the relative velocity for $\Omega_e = 4$ is plotted as a function of time. As illustrated in the figure, the relative velocity is at its highest near the location of the applied load and decreases towards the fixed end on the right, eventually reaching zero. As the relative velocity decreases, it becomes strictly positive, indicating the absence of sign changes and, consequently, no friction modulation. For $\Omega_e=2$ and $\Omega_e=3$, the relative velocity values remain strictly positive at all times, explaining the absence of friction modulation at any point x_c , as shown in Fig. 10(a).

When compared to the rigid rod case (load acting on the mass which oscillates on a rigid rod), the dot markers indicate lower average friction values for the rigid rod for all three Ω_e values (2, 3, and 4). Although the load in the rigid rod case is applied directly to the mass, while this section examines the scenario where the load is applied to the flexible rod, these cases are compared not only to highlight their differences but also because the rigid rod with the load on the mass serves as a benchmark for evaluating the effects of load application on the mass versus on the rod in flexible rod systems. For instance, as shown in Fig. 2(a), for $\Omega_e = 4$, when the load is applied to the mass in the flexible rod case, the average friction values are closer to those in the rigid rod case (with the load on the mass) and are even smaller along parts of the rod's length. In contrast, when the load is applied on the rod in the flexible rod case, Fig. 10(a), for $\Omega_e = 4$, the

average friction values are consistently higher than those in the rigid rod case (with the load on the mass). Thus, applying the load directly to the mass can result in greater friction modulation than applying it to the rod. The friction reduction increases as Ω_e increases to 5, 6 and 7, with the highest reduction for $\Omega_e = 6$, corresponding to the natural frequency of the rod's first mode, as shown in Fig. 10(a). For the latter case, the friction reduction associated with the flexible rod (green line) is greater than that of the rigid rod (green dot) and also greater than that of the load-on-mass case, where almost no friction reduction was observed (see Section 3.1). As already explained, for the load-on-mass case and for an excitation frequency of $\Omega_a = 6$, the rod velocity response is high and comparable to the mass response, but the two responses are in phase. This results in a low-magnitude relative velocity, predominantly positive, causing no change in the friction force's sign and, consequently, no friction modulation. In contrast, for the load-on-rod case described here, the rod's response is high while the mass response is minimal. As a result, the relative velocity is dominated by the rod's motion, leading to a change in the friction force's sign and a reduction in the average friction. For $\Omega_a = 5$ and $\Omega_a = 7$, the comparison varies depending on the position along the rod length.

It should be noted that for Ω_e values of 5, 6 and 7, the responses of the rod are high and do not comply with the small deformation theory. To accurately describe the system dynamics, geometric nonlinearity should be accounted for (see Appendix A.1). However, as large deformations are not desirable, another approach is to vary the excitation amplitude value, α , to identify the maximum α value that ensures the response complies with the small deformation theory. To achieve this, the results from Eqs. (12) and (13) using x_c as in Eq. (3) are compared to those from Eqs. (A.4) and (A.5) with x_c as in Eq. (4). Fig. 11(a) presents the average friction values corresponding to α values for which the results obtained from the equations of motion with and without geometric nonlinearity agree. As shown in the figure, for the results to agree, the α value is reduced from 0.004, used so far in this study, to 0.0015, 0.00004 and 0.001 for Ω_e values of 5, 6 and 7, respectively. For $\Omega_e=5$ and $\Omega_e=7$, the average friction changes along the beam length. The average friction values are smaller for the higher excitation frequency, but still bigger than those corresponding to the same Ω_a value in Fig. 10(a), as in the latter a greater α value is used. The reduction in α is most prominent for $\Omega_{\rho} = 6$, as this excitation frequency results in the highest rod displacement response. While the α reduction leads to small deformations, it also results in a relative velocity response with oscillation cycles having amplitudes smaller than the velocity v. Consequently, no friction change is present in sections along the rod length for $\Omega_o = 6$.

To provide an indication of the displacement values, Fig. 11(b) presents the maximum values of the displacement response across a range of velocities v for $\Omega_e=6$ and the reduced $\alpha=0.00004$. Within this velocity range, the peak displacement value is approximately 0.0022, corresponding to 0.22% of the rod's length L. This shows that as the excitation amplitude value is decreased, the strain value remains small and does not lead to failure phenomena. For comparison, in the next subsection, the scenario of maintaining the original α value while accounting for geometric nonlinearity is presented, along with the corresponding maximum deformation values.

To sum up, when the load is acting on the rod, the velocity response of the rod is higher than that of the mass and it increases as the excitation frequency increases, significantly contributing to friction reduction. This response changes along the rod length and exhibits oscillations at different frequencies leading to large variations in average friction values and in no variations towards the end of the rod. High responses also imply a potential deviation from the small deformation theory. To address this, either geometric nonlinearity should be incorporated into the model, or the amplitude of the harmonic load needs to be adjusted. A reduction of the α value implies less friction reduction. When the excitation frequency matches the natural frequency of the rod's first mode under a reduced α , this results in no friction reduction occurring in some sections along the length of the rod.

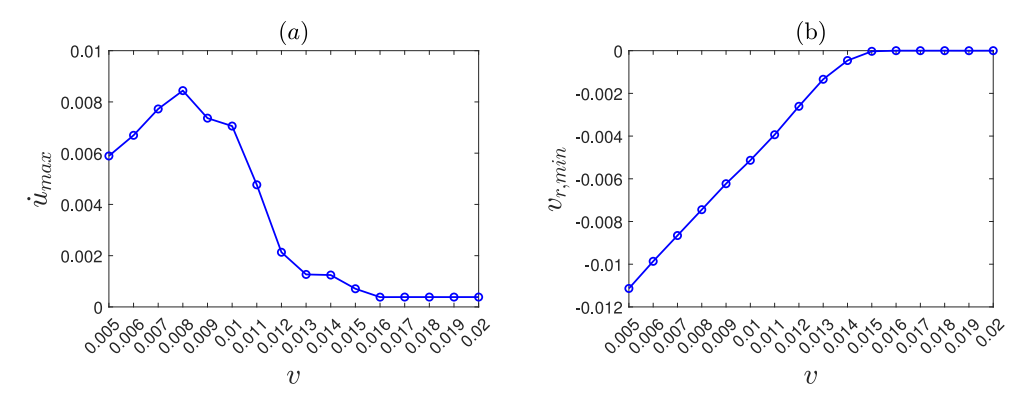


Fig. 8. (a) The maximum amplitude of the rod's velocity response at the contact point for different velocity v values and for $\Omega_e = 3$; (b) the minimum amplitude of the relative velocity response for the same parameter values.

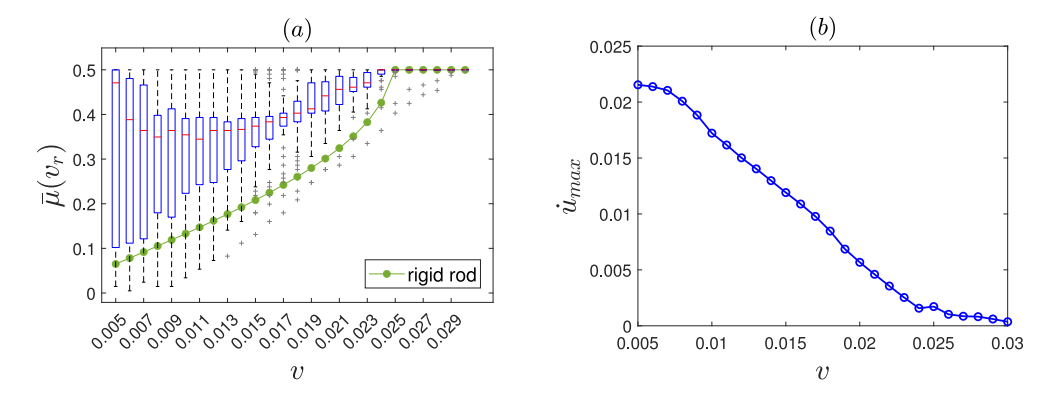


Fig. 9. (a) Comparison of average friction results for different velocity v values obtained for the flexible and rigid rod case for $\Omega_e = 6$; (b) Maximum amplitude of the rod's velocity response at the contact point.

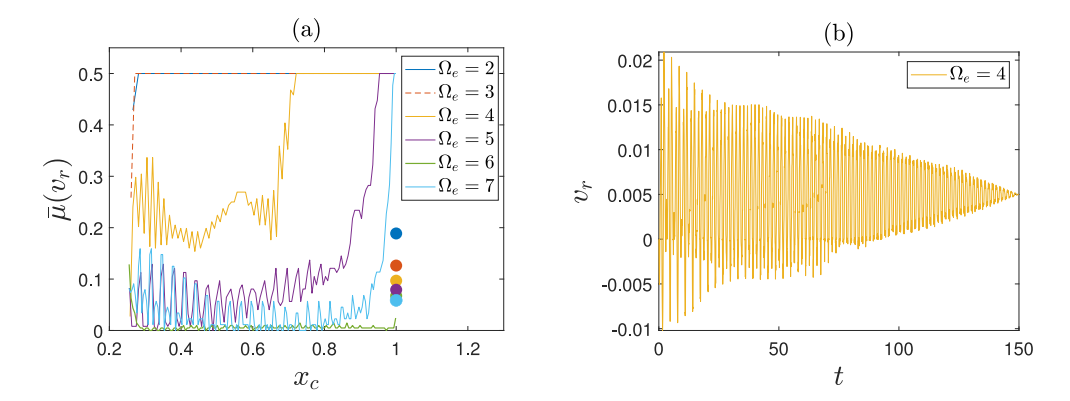
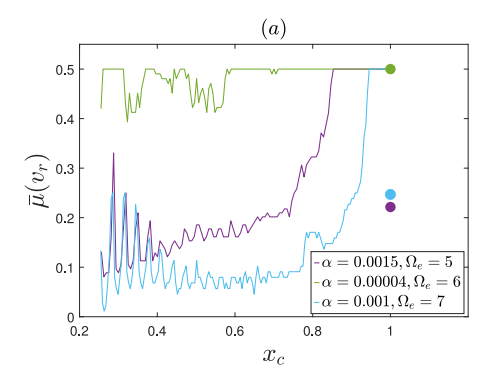


Fig. 10. (a) Average friction results along the rod length for different Ω_e values and v = 0.005. Continuous lines represent the results of the flexible rod and the dot markers those of the rigid rod. Dot marker colours match the lines for the same excitation frequency; (b) Relative velocity response for $\Omega_e = 4$.

4.2. Friction modulation versus pushing velocity

The average friction values for a range of velocities v are presented and compared for both the flexible and rigid rod cases. In Section 3.1, the comparison was made for excitation frequencies $\Omega_e=3$ and $\Omega_e=6$ for which the most significant differences between the flexible and rigid rod cases were observed. Looking at Fig. 10(a), for $\Omega_e=2$ and $\Omega_e=3$, no friction change is observed for v=0.005 and that holds for higher velocities as well since friction reduction lessens with increasing v. Therefore, no average friction plots are shown for these excitation frequencies. In Fig. 12(a), results for $\Omega_e=4$ are illustrated. As shown in the figure, the average friction values for the system with the flexible rod, except for some extremes, are higher than those for the rigid

rod system for any velocity v value. For the rigid rod, no change in friction is observed for $v \geq 0.018$, whereas for the flexible rod, this behaviour occurs at a lower v=0.014. The latter observation can be explained by revisiting the relative velocity response shown in Fig. 10(b) for v=0.005. As previously mentioned, the relative velocity decreases and becomes strictly positive as the mass approaches the fixed end of the rod, indicating no friction sign change and no friction modulation towards the rod's end. Increasing the velocity incrementally to v=0.006,0.007,..., up to v=0.02, as shown in Fig. 12(a), reduces the time required for the mass to reach the rod's end. For example, while the rod's end is reached at t=150 for v=0.005, it is reached at t=75 for v=0.01. With this shorter time frame and higher v values, the relative velocity response becomes strictly positive more



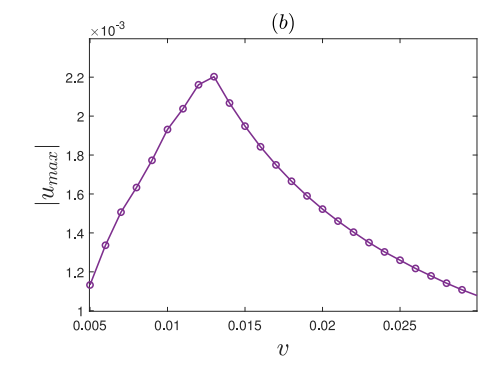
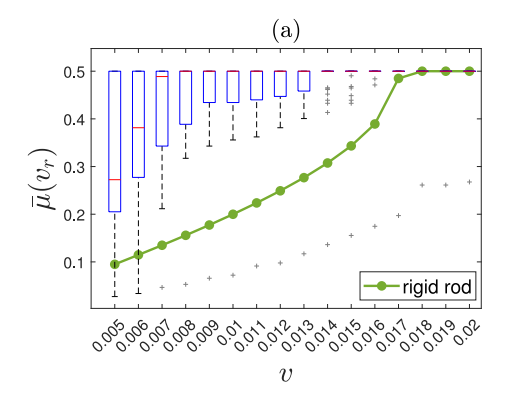


Fig. 11. (a) Average friction results along the rod length using α values for which the results from the equations of motion with and without geometric nonlinearity agree; (b) Maximum amplitude of the rod's displacement response for $\Omega_e = 6$ and $\alpha = 0.00004$.



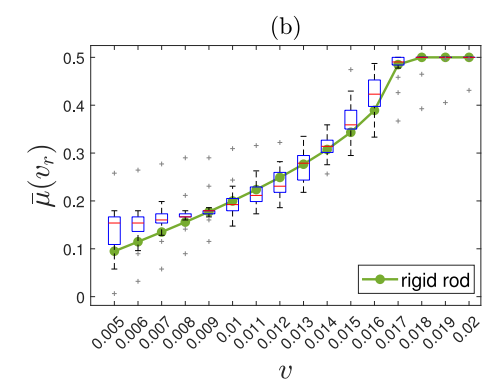


Fig. 12. Comparison of average friction results for different velocity v values obtained for the flexible and rigid rod case for $\Omega_e = 4$: (a) load acting on the rod, (b) load acting on the mass.

rapidly, occurring at $x_c \approx 0.5$ instead of approximately 0.7 (observed for v=0.005). Therefore, as the velocity v increases, no friction change is observed from lower x_c values.

In Fig. 12(b), the same plot is illustrated for the load-on-mass case, as studied in Section 3, with the boxplots showing again the results for the flexible rod system and the green markers the results for the rigid one (the latter being the same in Fig. 12(a) and 12(b)). As shown in the figure, the results align more closely with those of the rigid rod case as the mass governs the response, and the rod's contribution is minimal. Consequently, for this excitation frequency, applying the load directly to the mass yields average friction values similar to the rigid rod. In contrast, applying the load to the rod results in less reduction in friction, which diminishes rapidly as the velocity \boldsymbol{v} increases.

Using the same parameters and higher excitation frequencies, for the deformations to remain small, either the amplitude of the excitation α should get reduced, as shown in Fig. 11(a), or nonlinearity should be considered in the equations of motion. Using a smaller α , the reduction in friction for $\Omega_e = 6$ is not that significant (see Fig. 11(a)). Therefore, as shown in Fig. 13(a), the average friction is illustrated for the original value of $\alpha = 0.004$, $\Omega_e = 6$ and including the geometric nonlinearity in the rod. Since the excitation frequency matches the first mode of the rod, the velocity response amplitude of the rod becomes significantly higher ($\dot{u}_{\rm max} \approx 1$) compared to the constant velocity v. This leads to substantial friction reduction, as illustrated in Fig. 13(a). In contrast, for the rigid rod case, the average friction values are higher and no friction reduction is observed when $v \ge 0.025$. For the flexible rod, the average friction values remain low (due to the velocity amplitude of the rod being very large) with only small variations along each other for all the v values considered. Only for $v > \dot{u}_{max}$, no changes in the average friction will be observed for this case. To provide an indication of the displacement values, Fig. 13(b) presents the maximum values of the displacement response for the same range of velocities

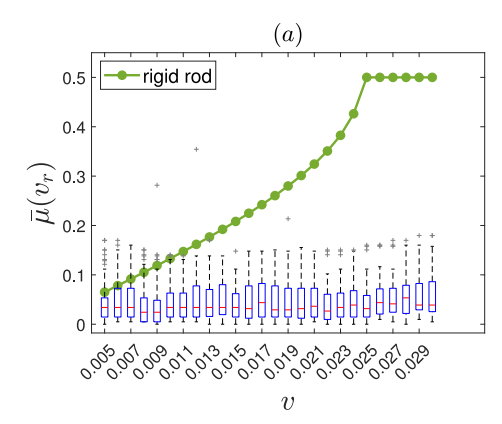
v as in Fig. 13(a). Within this velocity range, the peak displacement value is approximately 0.21, which is around 100 times larger than the one in Fig. 11(b) for the same excitation frequency but with a smaller amplitude α . This displacement is 21% L, and depending on factors such as material type, geometric properties (e.g., cross-sectional shape and size), loading conditions (e.g., magnitude, direction, and duration), boundary conditions and more, it can lead to failure phenomena such as buckling, permanent plastic deformation and crushing or fracture.

Overall, using an excitation frequency corresponding to the first mode results in greater friction reduction compared to the rigid case for any velocity v, but this comes with large deformations experienced by the flexible rod, where the material type and its properties play a crucial role.

5. Connection to real-life scenarios

5.1. Discussion on the slip joint application

In this section, connections are drawn to slip joints in offshore wind turbines and related experimental studies to contextualize the model system within the scope of applications and real-life scenarios. In the first study of Cabboi and coworkers on the slip joint application (Cabboi et al., 2020), the effectiveness of applying a harmonic excitation during the installation and decommissioning procedure was experimentally investigated using a 1:10 scaled model of the slip joint. In essence, a slip joint for wind turbines enables the connection between the monopile and the transition piece by simply overlapping the two cylindrical structures. The entire connection relies on the frictional forces between the two surfaces in contact. In their study, two cones, one representing the monopile (MP) and one the transition piece (TP), were used for the designed test setup. The TP was excited in either horizontal or vertical direction utilizing a shaker, whereas the static pushing load was applied



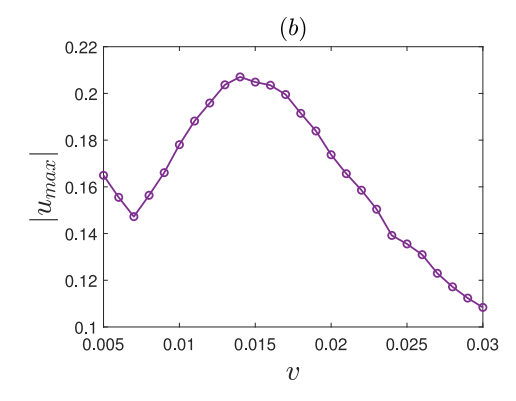


Fig. 13. Comparison of average friction results for different velocity v values obtained for the flexible rod with geometrical nonlinearity and rigid rod with the load acting on the mass; (b) Maximum amplitude of the rod's displacement response. Results obtained for $\Omega_e = 6$ and $\alpha = 0.004$.

at the top cone representing the MP. Both cones were made of the same steel type (S355), and had the same total length, mass and wall thickness. The TP cone had a top and bottom outer diameter of 0.01 m thicker than the MP cone. Due to its larger diameter, the TP cone was stiffer.

The results of the tests performed during the experimental campaign showed that settlement occurred when applying a harmonic load at specific forcing frequencies (results hold for both loading directions). To provide some insights concerning which structural modes should be excited to effectively obtain a stable settlement, hammer tests on the testing specimens and experimental modal analysis were performed. One of the identified natural frequencies, specifically at 120 Hz (whenever excited by means of the shakers), was effective in reducing the friction force for both the installation and dismounting of the cones, regardless of the different amplitudes of the vibratory load. However, settlements were observed for other frequencies as well, and in general, most of the settlement frequencies corresponded well with the identified natural frequencies.

Compared to our system, for the parameters considered, it can be verified that the rod has higher stiffness than the mass $(k_r = EA/L > k)$, allowing the rod to serve as a simplified representation of the TP. Similarly, the mass represents the MP for the considered test setup. While this setup simplifies the dynamics of the slip joint, it provides a foundational framework for analysis. As the excitation is applied on the TP, the corresponding case in our study is that of the load applied on the rod, as shown in Section 4. One of the conclusions of this section was that loading the rod with an excitation frequency corresponding to the rod's first mode leads to the highest friction reduction. The conclusion is similar to that drawn from the slip joint study as exciting the TP at resonance frequencies was the most effective way to install and decommission the connection.

In a follow-up study (Cabboi et al., 2021), the vibration-assisted decommissioning of the slip joint was applied to a full-scale wind turbine, where the lower tower of the wind turbine (WT) was directly connected to the monopile (MP) without the use of a transition piece. The wall thickness of the steel plates forming the monopile and the wind turbine tower decreased with increasing height, from 65 mm to 10 mm, making the MP the stiffer component. The shaker devices were mounted at the base of the wind turbine tower, so the vibratory load was applied to the WT. The decommissioning tests showed that the slip joint detachment was triggered once the circumferential local mode at 53 Hz was excited. An experimental modal analysis was conducted to identify the modes of the structure, and the results were compared to modal properties extracted from a developed FE model. This analysis showed that the mode at 53 Hz only referred to the dynamic of the wind turbine tower, while the monopile foundation almost acted as a rigid body. Thus, the excitation of this mode in combination with a vertical

pulling force facilitated the detachment between the two contacting surfaces.

Following the same line of reasoning as described above, compared to our system, the rod has higher stiffness, making it representative of the MP, and the mass representative of the WT, as the excitation is applied on the WT. The corresponding case in our study is of the load applied on the mass, see Section 3. This section concluded that exciting the mass at an excitation frequency corresponding to the rod's first mode results in less friction reduction. Thus, to reduce friction forces (i.e. to facilitate decommissioning), it is more effective to excite the mass at frequencies which do not correspond to the rod's first mode. In these cases, the rod response is generally small. This is in line with the result drawn by the study on the slip joint, as the decommissioning was effective at a frequency at which the monopile foundation, represented by the rod in our system, acted almost as a rigid body.

It should be noted that while our study and the slip joint application share conceptual similarities, the agreement between their results is purely qualitative. The slip joint primarily involves bending and circumferential shell modes, making an axially deforming rod not the most representative structure for comparison. Additionally, the dynamic loading in the slip joint study involves a stepwise or linear frequency increase, contrasting with the loading type used in our work. Differences in stiffness, damping ratios, and other parameters also show the distinct nature of the two systems, yet the qualitative agreements remain, highlighting the broader applicability of the findings.

5.2. Discussion on pin-on-disk experimental results

Lastly, a connection is drawn between the findings obtained in this study and related experimental works. In several experimental investigations conducted on the effect of vibration-induced friction reduction, the measurements did not match the model predictions obtained assuming the Amontons-Coulomb law to model the friction force. Different friction models were used to better catch the experimental behaviour, for example, the Dahl and the Dupont models (Dupont et al., 2002) that embed a tangential contact stiffness. In this regard, Kapelke employed the Dupont model and the Amontons-Coulomb law to compare the experimental results to theoretical ones (Kapelke and Seemann, 2018). A pin-on-disk type experimental setup was developed, exhibiting a dominant eigenmode at approximately 100 Hz (corresponding to the motion of the dynamometer in the tangential direction). For moderate excitation frequencies (40 Hz), the experimental results showed an excellent match to the elasto-plastic Dupont model, for which the contact stiffness $k_0 = 5.6 \times 10^5$ N/m was chosen. However, when highexcitation frequencies were used (350 Hz), to catch the behaviour of the friction force accurately, a significantly different value of tangential stiffness was needed for the Dupont model, i.e., $k_0 = 12 \times 10^5$ N/m.

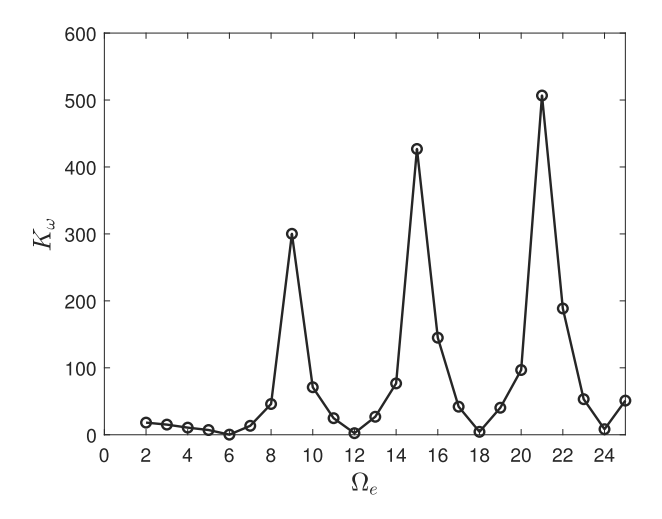


Fig. 14. "Dynamic stiffness" of the rod.

Since this model incorporates a tangential contact stiffness, and our system considers deformations in the tangential direction, a comparison can be made between the results obtained from both systems. As shown in Kapelke's work (Kapelke and Seemann, 2018), the elastoplastic friction model yields higher effective friction values than the Amontons-Coulomb law. The shape of the plots and the results are qualitatively similar to those shown in Fig. 7 (for v > 0.008) and in Fig. 9(a) (for any v), as these results are also higher than those obtained using the Amontons-Coulomb law. The comparison is made with these plots because they correspond to the scenario in which the harmonic load is applied to the mass, aligning with the experimental loading condition. It is important to note that a direct one-to-one comparison between the results from our mass-on-a-rod system and the system with the Dahl/Dupont models cannot be made, as additional information is needed regarding the relationship between the excitation frequency and the system modes, as well as consistent amplitude and velocity values. However, despite these limitations, our system demonstrates that using a rod with the Amontons-Coulomb law provides friction change results that qualitatively resemble those obtained from the Dahl/Dupont models.

An attempt to explain the need for a change in the contact stiffness value k_0 , as the excitation frequency increases, is made by calculating a "dynamic stiffness" (as perceived by the moving contact force throughout the transient process) of the rod in our system, K_{ω} . To compute K_{ω} , for a given excitation frequency, the force acting on the rod and the displacement at the contact point are transformed to the frequency domain. Due to the quasi-periodic nature of the system response, K_{ω} , which is the ratio of force to displacement amplitudes, also exhibits multiple frequency components. The K_{ω} value is then chosen based on the component that matches the given excitation frequency. The same procedure is repeated for other excitation frequencies, and the results are illustrated in Fig. 14. As shown in the figure, K_{ω} is at its lowest at the rod's modal frequencies and higher between them. Moreover, the peaks in the plot of K_{ω} increase with increasing frequency. This behaviour could explain why higher contact stiffness values are needed at higher excitation frequencies in the work of Kapelke and colleagues, assuming that the excitation frequency used in their study lies between the disk modes.

6. Conclusions

In this work, the effect of external excitation in the presence of support flexibility on the friction modulation of a moving oscillator on an elastic rod of finite length is investigated. Two loading scenarios are analysed. In the first, a harmonic tangential load is applied on the

moving mass, while in the second, the same load is applied on the rod. The modal expansion method is employed to derive the modal equations of the rod, which are then used to obtain the numerical solutions for the system's response.

In the case where the load acts on the mass, it is observed that, unlike the rigid rod scenario where the average friction is a constant value, the deformation of the rod introduces variations in friction change along its length. Depending on the position along the rod length, these values are smaller or bigger than the ones obtained for the rigid rod system. Deviations are observed across excitation frequencies, with the most prominent ones occurring at half the rod's first mode frequency and at the first mode frequency itself. For the latter case, unlike the rigid rod scenario, no friction modulation and stick-slip behaviour is observed along parts of the rod. For both cases, it is also found that the critical velocity, i.e. the velocity for which the maximum rod velocity response is observed, provides direct qualitative insight into the differences in average friction between the rigid and flexible rod cases without explicitly computing the average friction values for the latter scenario. For pushing velocities smaller than the critical velocity, the average friction values for the flexible rod are lower than those of the rigid case, while above it, the opposite is true.

Even when the load acts on the rod, variations in average friction values along the rod length are observed, but they differ from the results from the load-on-mass scenario. For excitation frequencies close to and above the rod's first natural frequency, the rod's response increases and does not comply with the small deformation theory. To address this, either the amplitude of the excitation value α is reduced, or, if large deformations are permitted, geometric nonlinearity is incorporated into the model. A lower α value leads to less friction reduction for all excitation frequencies and to no friction reduction along parts of the rod for the excitation frequency equal to the rods' first natural frequency. For the same excitation frequency, introducing geometric nonlinearity results in very high friction reduction compared to the rigid case for any velocity v. Again, this comes with large deformations experienced by the flexible rod.

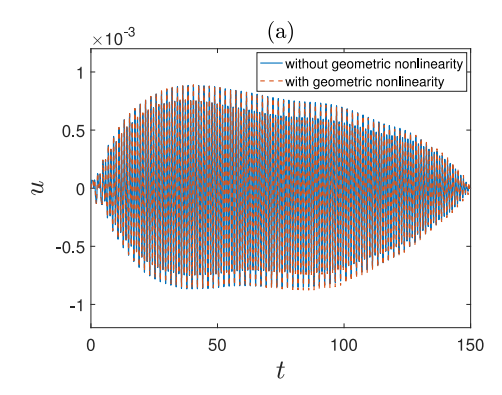
The presence of support flexibility allows for comparisons with real-life applications as well. Regarding the slip joint application, the system's behaviour is used to represent a simplified version of the dynamics of the tower and the monopile. The findings from our study regarding the choice of excitation frequencies for which the highest friction reduction is obtained in the load-on-mass and load-on-rod scenarios support the results of the experiments on the full scale and on the 1:10 scaled model of the slip joint, respectively. Regarding experimental studies, the average friction results from our study are used to provide an alternative interpretation of the results of published works using the Dahl and Dupont models. Using these models, higher average friction values than those predicted by Amontons-Coulomb law are observed. Similarly, in our study, according to a comparable loading scenario, higher average friction values are also observed (depending on the excitation frequency and pushing velocities). Thus, modelling the system with a flexible rod yields friction change results that qualitatively align with those from the Dahl and Dupont models and related experimental studies, even though the Amontons-Coulomb law is used.

CRediT authorship contribution statement

E. Sulollari: Writing – review & editing, Writing – original draft, Visualization, Software, Methodology, Investigation, Formal analysis, Conceptualization. K.N. van Dalen: Writing – review & editing, Supervision, Methodology. A. Cabboi: Writing – review & editing, Supervision, Methodology.

Declaration of competing interest

The authors declare that they have no known competing financial interests or personal relationships that could have appeared to influence the work reported in this paper.



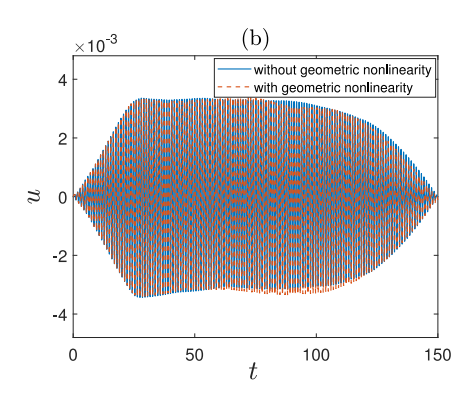


Fig. A.15. Comparison of rod displacement u obtained using the equations of motion with (dashed orange line) and without (continuous blue line) geometric nonlinearity in the rod; (a) for excitation frequency $\Omega_e = 3$, (b) for excitation frequency $\Omega_e = 6$.

Appendix

A.1. Geometrically nonlinear rod

With reference to Section 3.1, to ensure that the response of the rod adheres to the small deformation assumption, the solutions obtained are compared to those derived considering a rod with geometric nonlinearity with x_c expression as in Eq. (4). For the geometrically nonlinear rod, the displacement-strain relation (de Borst et al., 2012) and the strain-stress relation are given by

$$\varepsilon_x = \frac{\partial u}{\partial x} + \frac{1}{2} \left(\frac{\partial u}{\partial x} \right)^2, \quad \sigma_x = E \varepsilon_x.$$
 (A.1)

Thus, the displacement-strain relation has an additional quadratic term. The equations of motion then become

$$\rho A \frac{\partial^2 u}{\partial t^2} + c_b \frac{\partial u}{\partial t} - EA \frac{\partial^2 u}{\partial x^2} - EA \frac{\partial u}{\partial x} \frac{\partial^2 u}{\partial x^2} + f \delta(x - x_c) = 0, \tag{A.2}$$

$$m\frac{d^2u}{dt^2} + c\frac{du}{dt}s + ks = f, (A.3)$$

Using the same dimensionless parameters as in Eq. (9), the dimensionless equation of motion are derived

$$\frac{\partial^2 u}{\partial t^2} + 2\beta_b r_w \frac{\partial u}{\partial t} - \left(\frac{r_\omega}{\pi}\right)^2 \frac{\partial^2 u}{\partial x^2} - \left(\frac{r_\omega}{\pi}\right)^2 \frac{\partial u}{\partial x} \frac{\partial^2 u}{\partial x^2} + f\delta(x - x_c) = 0, \quad (A.4)$$

$$\frac{d^2u}{dt^2}s + 2\beta\frac{du}{dt} + s = r_m f,$$
(A.5)

The modal equations of the rod are derived using the same solution method as in Section 3.1 and are solved numerically using the MATLAB solver ode23s.

In Fig. A.15, the results of the rod displacement u obtained using the equations of motion with (dashed orange line) and without (continuous blue line) geometric nonlinearity of the rod are presented for two different excitation frequencies. As shown in Fig. A.15(a) for $\Omega_e=3$, the differences between the lines are negligible. The differences become more pronounced at higher time values for $\Omega_e=6$, as shown in Fig. A.15(b). This case is particularly noteworthy since $\Omega_e=6$ corresponds to the first natural frequency of the rod, leading to a higher response. Nevertheless, the maximum relative error in the responses is approximately 6.7%, and this occurs only within a narrow time range. As a result, the error has no significant impact on the relative velocity and, consequently, on the average friction.

Data availability

Data will be made available on request.

References

Amontons, G., 1699. De la resistance cause'e dans les machines (about resistance and force in machines). Mem L' Acedemie R A 257-282.

Argatov, I., Papangelo, A., Ciavarella, M., 2025. An asymptotic model of vibroadhesion. Int. J. Non-Linear Mech. 136, 105089.

Cabboi, A., Kamphuis, T., van Veldhuizen, E., Segeren, M., Hendrikse, H., 2021. Vibration-assisted installation and decommissioning of a slip-joint: Application to an offshore wind turbine. Eng. Struct. 76 (102931).

Cabboi, A., Segeren, M., Hendrikse, H., Metrikine, A., 2020. Vibration-assisted installation and decommissioning of a slip-joint. Eng. Struct. (ISSN: 0141-0296) 209, 109949.

Cabboi, A., Woodhouse, J., 2018. Validation of a constitutive law for friction-induced vibration under different wear conditions. Wear 396–397. 107–125.

Cabboi, A., Woodhouse, J., 2020. Identifying short-term variation of dynamic friction by means of its frequency response function. J. Sound Vib. 472 (115212).

Costagliola, G., Bosia, F., Pugno, N., 2017. Hierarchical spring-block model for multiscale friction problems. ACS Biomater. Sci. Eng. 3 (11), 2845–2852.

Costagliola, G., Bosia, F., Pugno, N., 2018. A 2-D model for friction of complex anisotropic surfaces. J. Mech. Phys. Solids 112, 50-65.

Coulomb, C.A., 1821. Theorie des Machines Simple (Theory of Simple Machines). Bachelier, Paris.

Dahl, R.P., 1976. Solid friction damping of mechanical vibrations. AIAA J. 14 (12), 1675–1682.

de Borst, R., Crisfield, M., Remmers, J., Verhoosel, C., 2012. Non-Linear Finite Element Analysis of Solids and Structures, second ed Wiley, Chichester, p. 544.

Dupont, P., Hayward, V., Armstrong, B., Altpeter, F., 2002. Single state elastoplastic friction models. IEEE Trans. Autom. 47 (5), 787–792.

Fărăgău, A.B., Mazilu, T., Metrikine, A.V., Lu, T., van Dalen, K.N., 2021. Transition radiation in an infinite one-dimensional structure interacting with a moving oscillator—the Green's function method. J. Sound Vib. 492, 115804.

Frýba, L., 1973. Vibration of Solids and Structures Under Moving Loads. vol. 1, Springer.

Grudziński, K., Kostek, R., 2007. An analysis of nonlinear normal contact microvibrations excited by a harmonic force. Nonlinear Dynam. 50 (4), 809–815.

Hess, D.P., Soom, A., Kim, C., 1992. Normal vibrations and friction at a Hertzian contact under random excitation: Theory and experiments. J. Sound Vib. 153 (3), 491–508.

Hoffmann, N., Wagner, N., Gaul, L., 2005. Quenching mode-coupling friction-induced instability using high-frequency dither. J. Sound Vib. 279 (1), 471–480.

Hong, J., Kim, J., Chung, J., 2020. Stick-slip vibration of a moving oscillator on an axially flexible beam. J. Mech. Sci. Technol. 34, 541–553.

Ipri, S.L., Asada, H.H., 1995. Tuned dither for friction suppression during force-guided robotic assembly. In: Proc. 1995 IEEE/RSJ Int. Conf. on Intell. Robots and Systems. Human Robot Interaction and Cooperative Robots. vol. 1, pp. 310–315.

Kapelke, S., Seemann, W., 2018. On the effect of longitudinal vibrations on dry friction: Modelling aspects and experimental investigations. Tribol. Lett. 66 (3).

Kumar, V., Hutchings, I., 2004. Reduction of the sliding friction of metals by the application of longitudinal or transverse ultrasonic vibration. Tribol. Int. 37 (10), 833–840.

Li, Z., Ouyang, H., Guan, Z., 2016. Nonlinear friction-induced vibration of a Slider–Belt system. J. Vib. Acoust. 138.

Littmann, W., Storck, H., Wallaschek, J., 2001. Proceedings of the SPIE, volume 4331, 302–311. In: SPIE Proceedings. vol. 4331, pp. 302–311.

Liu, H., Yang, B., Wang, C., Han, Y., Liu, D., 2022. The mechanisms and applications of friction energy dissipation. Friction 11 (6), 839–864.

Menga, N., Bottiglione, F., Carbone, G., 2021. Dynamically induced friction reduction in micro-structured interfaces. Nature 11 (1), 171–184.

- Menga, N., Bottiglione, F., Carbone, G., 2023. Exploiting surface textures dynamics for dry friction control. Nonlinear Dynam. 111, 3099–3112.
- Meyer, D.J., Wiertlewski, P., A., M., Colgate, J.E., 2014. Dynamics of ultrasonic and electrostatic friction modulation for rendering texture on haptic surfaces. IEEE Haptics Symp..
- Michaux, M.A., Ferri, A.A., Cunefare, K.A., 2007. Effect of tangential dither signal on friction induced oscillations in an SDOF model. J. Comput. Nonlinear Dyn. 2, 201–210.
- Ouyang, H., Mottershead, J., Cartmell, M., Brookfield, D., 1999. Friction-induced vibration of an elastic slider on a vibrating disc. Int. J. Mech. Sci. 41, 325–336.
- Siegert, K., Möck, A., 1996. Wire drawing with ultrasonically oscillating dies. J. Mater. Process. Technol. 60 (1–4), 657–660.
- Sinou, J., Jezequel, L., 2007. Mode coupling instability in friction-induced vibrations and its dependency on system parameters including damping. Eur. J. Mech. A Solids 26, 106–122.
- Soom, A., Kim, C., 1983. Interactions between dynamic normal and frictional forces during unlubricated sliding. J. Lubr. Technol. 105 (2), 221–229.
- Storck, H., Littmann, W., Wallaschek, J., Mracek, M., 2002. The effect of friction reduction in presence of ultrasonic vibrations and its relevance to travelling wave ultrasonic motors. Ultrasonics 40 (1), 379–383.

- Sulollari, E., van Dalen, K.N., Cabboi, A., 2024. Vibration-induced friction modulation for a general frequency of excitation. J. Sound Vib. 573.
- Sulollari, E., van Dalen, K.N., Cabboi, A., 2025. Parametric excitation and friction modulation for a forced 2-DOF system. Nonlinear Dynam. 113, 12793-1281.
- Thomsen, J.J., 1999. Using fast vibrations to quench friction-induced oscillations. J. Sound Vib. 228 (5), 1079–1102.
- Tolstoi, D., 1967. Significance of the normal degree of freedom and natural normal vibrations in contact friction. Wear 10 (3), 199–213.
- Tricarico, M., Ciavarella, M., Papangelo, A., 2025. Enhancement of adhesion strength through microvibrations: Modeling and experiments. J. Mech. Phys. Solids 196, 106020
- Tsai, C., Tseng, C., 2006. The effect of friction reduction in the presence of in-plane vibrations. Arch. Appl. Mech. 75, 164–176.
- Tsetas, A., Tsouvalas, A., Gómez, S.S., Pisanò, F., Kementzetzidis, E., Molenkamp, T., Elkadi, A.S.K., Metrikine, A.V., 2023. Gentle driving of piles (GDP) at a sandy site combining axial and torsional vibrations: Part I - installation tests. Ocean Eng. 270 (113453).